Ocean Engineering 141 (2017) 450–464

Contents lists available at ScienceDirect

Ocean Engineering

journal homepage: www.elsevier.com/locate/oceaneng

CFD simulations of free running ship under course keeping control

Jianhua Wang, Lu Zou, Decheng Wan*

School of Naval Architecture, Ocean and Civil Engineering, State Key Laboratory of Ocean Engineering, Shanghai Jiao Tong University, Collaborative Innovation Center for Advanced Ship and Deep-Sea Exploration, 800 Dongchuan Road, Minhang District, Shanghai 200240, China

ARTICLE INFO

Keywords:
Free running ship
Course keeping
Overset grid
naoe-FOAM-SJTU solver

ABSTRACT

The free running ONR Tumblehome ship model is numerically studied under course keeping control. Simulations are carried out using naoe-FOAM-SJTU, a CFD solver developed on open source platform OpenFOAM. Overset grid technique and 6DOF module with a hierarchy of bodies are applied to handle the free running ship motions with twin actual rotating propellers and moving rudders. Self-propulsion computation in calm water is first performed to achieve the approach speed (U=1.11 m/s, Fr=0.2) using a proportional-integral controller. The obtained self-propulsion model point is then used for the free running computation under course keeping control in waves, where three regular waves are considered: head wave, bow quartering wave and beam wave. To fulfil the course keeping demand, a new course keeping control module is developed using feedback controller based on the CFD solver naoe-FOAM-SJTU. The predicted results are compared with the benchmark data in Tokyo 2015 CFD Workshop in ship hydrodynamics. Good agreements are achieved for both self-propulsion and course keeping tests, which shows that free running ship simulations especially in waves using the CFD approach coupled with newly developed course keeping module is feasible and reliable. Furthermore, flow visualizations are also presented to explain the hydrodynamic performance of ship hull-propeller-rudder interaction in waves under course keeping conditions.

1. Introduction

A vessel in real sea states is preferable to sail straight forward with the consideration of less operational costs. However, the behavior of a vessel is strongly relied on the sea environment, where the path of the vessel may deviate from the original course due to the external forces by waves, currents and winds. The course keeping behavior of ships should not be neglected and the idea of this lead to the IMO standards and criteria (International Maritime Organization, 2002). Thus, how to evaluate the course keeping ability under rough sea states at the design stage is of paramount importance. The course keeping behavior of a vessel becomes even more complicated when encountering oblique waves. The sea waves can strongly affect the path of an advancing ship and thus reasonable course control is encouraged to maintain the straight-line stability. The accurate prediction of this phenomenon appears to be an essential need.

In general, there are several approaches to predict the maneuvering and seakeeping behavior of free running ships. Traditional experiment test still plays an important role in this area, where the measurement facility is improved significantly in order to keep pace with the increasing requirement of free running model tests. Extensive experiments have been done at the Iowa Institute of Hydraulic Research (IIHR) wave basin for free running models in different conditions (Araki et al., 2012; Sanada et al., 2013), in which the experimental data of course keeping can be found in Tokyo 2015 CFD workshop in ship hydrodynamics. Although experiments can give reliable results, high cost and complexity in local flow measurement still hold back its application and are always required only at the final design stage. Numerical methods have been used in predicting these problems. System based simulations (SBS) (Sakamoto et al., 2012; Simonsen et al., 2012) and potential methods are very fast to give predicted results. However, since both of them rely on the simpler mathematical modeling, it is difficult to resolve the complex flow around rotating propellers and moving rudders. CFD method becomes an attractive approach in prediction of ship maneuvering and seakeeping due to the fact that viscous effects are important in these conditions. Tezdogan et al. (2015) presented detailed procedures for the CFD prediction of ship response to waves using fully nonlinear unsteady RANS method. Ship motions and resistance were underpredicted and all numerical results fell within circa 10% of those from experiments. The authors also states that the study should be extended to incorporate the propeller and appendages, as these will also have a notable effect on ship behavior and performance.

Direct CFD simulations, which adopt the actual rotating propellers

* Corresponding author.
E-mail address: dcwan@sjtu.edu.cn (D. Wan).

http://dx.doi.org/10.1016/j.oceaneng.2017.06.052
Received 28 February 2017; Received in revised form 15 May 2017; Accepted 21 June 2017
Available online 05 July 2017

and moving rudders with no simplifications, are able to provide accurate prediction of hydrodynamic locals and specific local flow details due to the capability of resolving the complex flow among the rotating propellers, moving rudders, and ship hull. However, due to the high computational cost and complex modeling, up until now still quite few free running simulations have been performed, especially for the free running ship in waves.

To perform free running CFD simulations, the most reliable and robust approach so far is the dynamic overset grid method coupled with full 6DoF motion solver with a hierarchy of bodies. The approach was first successfully introduced to naval architecture for CFD simulations of self-propulsion ships. Carrica et al. (2010) used a speed controller and a discretized propeller with dynamic overset grids to directly perform the self-propulsion computations. The single-propeller KVLCC1 tanker appended with a rudder, the twin propeller fully appended surface combatant model DTMB 5613, and the KCS container ship without a rudder, were evaluated. Good agreements with experimental data were achieved, which showed that direct computation of self-propelled ships is feasible. Castro et al. (2011) investigated the full-scale computations for self-propelled KRISO container ship KCS using discretized propeller model, and gave the conclusion that the propeller operates more efficiently in full scale and is subject to smaller load fluctuations.

With the improvements of dynamic overset grids, direct simulations of ship maneuvers with active rudders become feasible. Mofidi and Carrica (2014) presented the direct simulation of zigzag maneuver for a container ship, where standard 10/10 zigzag maneuver and modified 15/1 zigzag maneuver were computed. Good agreement with the experiment data was achieved and the authors emphasized that the computational cost in direct calculating free running ships was still very high. Broglia et al. (2015) and Dubbioso et al. (2016) used a similar overset grid approach to simulate the turning circle maneuver of a fully appended twin screw vessel using a finite volume method CFD solver. Further analysis for the distribution of forces and moments on the hull, appendages and rudders was done to obtain the hydrodynamic behavior in turning tests. Shen et al. (2015) implemented the dynamic overset grid module to OpenFOAM and formed the ship hydrodynamic CFD solver naoe-FOAM-SJTU. The solver is successfully applied to the KCS self-propulsion and zigzag maneuvering simulation. Unlike previous studies, the unstructured overset grid technique was introduced for marine applications and the method showed good flexibility and efficiency of the mesh generation for complex geometries. The predicted results showed good agreements with the experimental data, indicating that the fully discretized model with overset grid method was feasible even for the relatively coarse unstructured grids. Wang et al. (2016) used the same solver naoe-FOAM-SJTU to simulate the turning circle maneuver of the ONR Tumblehome model in calm water, and the predicted ship motions for the maneuvering conditions agree well with the available experimental data.

Previous studies for free running ship with actual rotating propellers and moving rudders are mostly focused on the calm water and few researches of free running ship in waves have been done. In this paper, an incompressible RANS approach with dynamic overset grid method is applied for all the simulations. A course keeping control module is developed to simulate the free running ship model under course keeping control in different heading waves. The present paper is divided as follows. The first part deals with the prediction of free running ships in general context of available methods. The second section presents the numerical approach, where the CFD solver naoe-FOAM-SJTU, dynamic overset grid and course keeping module, wave generation and absorption are discussed in detail. The third part is the geometry, grid and simulation design, including the geometry model, grid distribution and test conditions. Then comes the simulation results and analysis section, where numerical results of self-propulsion in calm water and in different waves are presented and compared with the experimental measurement. Finally, the conclusions of this study are summarized.

2. Numerical approach

2.1. naoe-FOAM-SJTU solver

The computations are performed with the ship hydrodynamics CFD code, naoe-FOAM-SJTU, developed on open source platform, OpenFOAM (2016). The latest version of naoe-FOAM-SJTU is based on OpenFOAM version 3.0.1. The solver has been extensively validated on large amount of ship hydrodynamic cases, e.g. ship resistance (Zha et al., 2015), seakeeping (Shen et al., 2014; Shen and Wan, 2013) and maneuvering (Shen et al., 2015; Wang et al., 2016). Only the key points are recalled here and the details are presented in Shen et al. (2012).

The present solver mainly consists of an overset grid module, a full 6DoF motion module with a hierarchy of bodies (Shen et al., 2015) and a 3-dimensional wave generation and absorption module (see Section 2.3). naoe-FOAM-SJTU solves the Reynolds-averaged Navier-Stokes (RANS) equations for unsteady turbulent flows around the complex geometry models. The turbulence is modeled by a blended $k-\omega/k-\varepsilon$ shear stress transport (SST) turbulence model (Menter et al., 2003). Wall functions are used to model the velocity gradient effects near wall. The volume of fluid (VOF) approach with bounded compression technique is used to capture free surface (Weller, 2008).

Finite volume method (FVM) with fully unstructured grids is used to transform the equations from physical space into computational space. The solution of the governing equations is achieved by using the pressure-implicit split-operator (PISO) algorithm (Issa, 1986). Furthermore, several built-in numerical schemes in OpenFOAM are used to solve the partial differential equations (PDE). The Euler scheme is used for temporal discretization. Second order Total Variation Diminishing (TVD) scheme is used to discretize the convection term, while a central differencing scheme is applied for diffusion terms.

2.2. Dynamic overset grid and course keeping module

This section details the dynamic overset grid technology and full 6DoF motion solver with a hierarchy of bodies. The dynamic overset grid is the key point for direct simulating the complex ship motions with moving components, i.e. propellers and rudders. Generally, overset grid includes two or more blocks of overlapping structured or unstructured grids, and the overlapping grids can move independently without any constraints. In the overset calculation process, the grids in the computational domain are first merged together and classified into several types according to their locations, e.g. fringe cell, hole cell, donor cell, active cell and orphan. Fringe cell has a stencil consisting of several donor cells that provide information to it from the donor grid. The value of a flow variable ϕ of the fringe cell is obtained by interpolation from the donor cells:

$$\phi = \sum_{i=1}^{n} \omega_i \cdot \phi_i \tag{1}$$

$$\sum_{i=1}^{n} \omega_i = 1 \tag{2}$$

where ω_i is the weight coefficient and ϕ_i is the flow value from the donor cell i. The information mentioned above, i.e. cell types and interpolation coefficients are called the domain connectivity information (DCI). In the present work, Suggar++ library (Noack et al., 2009) is utilized to obtain the DCI at run time. To combine OpenFOAM with Suggar++, a communication, which is responsible for DCI exchange between OpenFOAM processor and Suggar++ processor, has been implemented using the message passing interface (MPI) library. Other features consist of a full 6DoF motion module with a hierarchy moving components and several modifications for sparse matrix solvers and

MULES solver to excluded non-active cells (fringe, hole, and orphan cells).

Full 6DoF motion solver with the dynamic overset grid capability allows the ship hull as well as the moving components to move simultaneously. Two coordinate systems are used to solve the 6DoF equations. One is the inertial system (earth-fixed system) and the other is non-inertial system (ship-fixed system). The inertial system can be fixed to earth or move at a constant speed with respect to the ship but not allowed to pitch, heave or roll so that can keep the free surface horizontal. The non-inertial system is fixed to the ship and can translate or rotate according to its motions. Details of the 6DoF motion with a hierarchy of bodies and overset grid module implementation can be found in Shen et al. (2015). In our present study, the complex geometry is decomposed into several overlapping grids, and can be used to handle complex ship motions with moving components.

Feedback controllers are used for self-propulsion, heading control under specified requirement of ship motion. A proportional-integral (PI) controller is implemented to act on the propeller to achieve the target speed for self-propulsion computations (Shen et al., 2015).

A course keeping module is developed to extend the capability of previous CFD solver naoe-FOAM-SJTU (Section 2.1) in simulating free running ship under course keeping control. The rudder is controlled by the feedback controller, where the rudder is executed according to the deviation of yaw angle from target heading angle. The control mechanism is as follows:

$$\delta(t) = K_P(\psi(t) - \psi_C) \tag{3}$$

where $\delta(t)$ is the rudder angle, K_P is proportional gain, and the present value is set to 1.0 according to the experiment. ψ_C is the target yaw angle and $\psi(t)$ is the instantaneous yaw angle during ship advancing in waves.

2.3. Wave generation and absorption

The self-developed numerical wave tank module in naoe-FOAM-SJTU solver is used to generate desired waves environment. Only a brief introduction is presented herein, and detailed information can be referred to Can and Wan (2014, 2015) and Shen and Wan (2016). The schematic of the wave generation and absorption for different directions is shown in Fig. 1. A fixed inlet wave boundary condition is applied to generate desired waves. Boundary conditions of $\boldsymbol{U}(u, v, w)$ in RANS equations can be directly adopted as the Dirichlet condition with specified wave theory. First order Stokes wave theory in deep water is adopted herein, and the expressions are as follows:

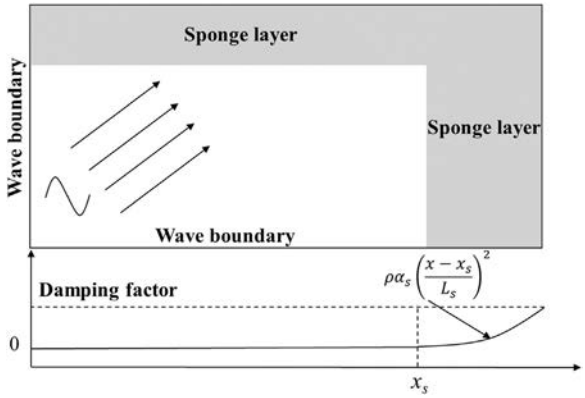

Fig. 1. Schematic of the wave generation and absorption.

$$\begin{cases} \eta = a\ \cos(\boldsymbol{k}\cdot\boldsymbol{x} - \omega\ t + \delta) \\ u = a\omega\ e^{kz}\cos(\boldsymbol{k}\cdot\boldsymbol{x} - \omega\ t + \delta) \\ v = a\omega\ e^{kz}\cos\chi\ \cos(\boldsymbol{k}\cdot\boldsymbol{x} - \omega\ t + \delta) \\ w = a\omega\ e^{kz}\sin\chi\ \cos(\boldsymbol{k}\cdot\boldsymbol{x} - \omega\ t + \delta) \end{cases} \tag{4}$$

where η is the desired wave elevation and u, v, w is the wave velocity boundary condition, $\boldsymbol{k}$ is the wave number presented as a vector that includes wave direction. δ is the wave phase determine the initial state of the incident waves, for example, the wave crest is located at FP of the ship at the beginning of simulation. χ is the wave direction defined as the angle between the ship advancing direction and the wave direction. For instance, $\chi = 0$ is head wave and $\chi = 90$ is beam wave.

The boundary condition for α is more complicated compared with the velocity boundary. When the cell of the inlet boundary is totally below the transient wave elevation, then the value of α is 1, otherwise α is 0. If the wave elevation is across the boundary cell, then α can be obtained as:

$$\alpha = \frac{S_w}{S_0} \tag{5}$$

where S_0 is the total area of the cell face and S_w is the wetted face area.

A wave damping zone, also called the sponge layer is set ahead the outlet boundary with a certain length. In the damping zone, the wave can be absorbed by adding a source term in momentum equation, which is denoted as:

$$fs(x) = \begin{cases} -\rho\alpha_s\left(\frac{x-x_s}{L_s}\right)^2(\boldsymbol{U} - \boldsymbol{U_{ref}}) \\ 0 \end{cases} \tag{6}$$

The distribution of the wave damping factor along the wave tank is shown in Fig. 1. This method has been extensively validated in the previous work (Cao and Wan, 2014, 2015; Shen and Wan, 2016).

3. Geometry, grid and simulation design

3.1. Geometry model

The ONR Tumblehome model 5613, which is a preliminary design of a modern surface combatant fully appended with skeg and bilge keels, is employed for all the free running simulations. In addition, the model is equipped with twin rudders, shafts and twin propellers with propeller shaft brackets. The geometry model of ONR Tumblehome is shown in Fig. 2, and the principle geometric characteristics both in model scale and full scale are listed in Table 1. The ship model is used as one of the benchmark cases in Tokyo 2015 CFD workshop in ship hydrodynamics and EFD results are also available for the free running tests.

3.2. Grid distribution

In the present study, the computational domain is divided into six parts: one for the background grid, one for grid around ship hull, two for the grids around propeller in starboard side and port side, two parts for both side rudders. For the overset grid arrangement, the background domain extends to $-1.5\ L_{WL} < x < 3.0\ L_{WL}$, $-1.5\ L_{WL} < y < 1.5\ L_{WL}$, $-1.0\ L_{WL} < z < 0.5\ L_{WL}$, and the hull domain is much smaller with a range of $-0.15\ L_{WL} < x < 1.2\ L_{WL}$, $-0.13\ L_{WL} < y < 0.13\ L_{WL}$, $-0.2\ L_{WL} < z < 0.2\ L_{WL}$.

Fully unstructured grids are generated by *snappyHexMesh* with the

Fig. 2. Geometry model of ONR Tumblehome.

Table 1
Main particulars of ONR Tumblehome model.

Main particulars	Symbols	Model scale	Full scale
Length of waterline	$L_{WL}(m)$	3.147	154.0
Maximum beam of waterline	$B_{WL}(m)$	0.384	18.78
Draft	T (m)	0.112	5.494
Displacement	Δ (kg)	72.6	8.507e6
Wetted surface area (fully appended)	$S_0(m^2)$	1.5	NA
Block coefficient	$\nabla/(L_{WL}B_{WL}T)$	0.535	0.535
Longitudinal center of gravity	$LCB(m)$ aft of FP	1.625	NA
Vertical center of gravity	$KG(m)$	0.156	NA
Moment of inertia	K_{xx}/B	0.444	0.444
	K_{yy}/L_{WL}, K_{zz}/L_{WL}	0.246	0.25
Propeller diameter	$D_P(m)$	0.1066	NA
Propeller shaft angle (downward positive)	e(deg.)	5	NA
Propeller rotation direction (view from stern)		inward	inward
Maximum rudder rate	(deg. /s)	35.0	NA

Table 2
Grid information in each part.

Grid	Total	Port	Starboard	Level
Background	1.36–1.64 M[a]	NA	NA	Root
Hull	2.61 M	NA	NA	Parent
Propeller	2.28 M	1.14 M	1.14 M	Children
Rudder	0.58 M	0.29 M	0.29 M	Children
Total	6.83–7.11 M[a]	NA	NA	NA

[a] Background grids for calm water case and wave case are 1.36 M and 1.64 M.

background grid generated by *blockMesh*, both are pre-processing utilities provided by OpenFOAM. The *blockMesh* tool generates the Cartesian background grid and *snappyHexMesh* tool refines the grids by splitting cells. Overset grid topology at solid surfaces and cross-sections is shown in Fig. 3. Five boundary layers on solid surfaces with extension of 1.2 are set and the final y^+ is 30–60, making the first cell outside the walls is in the log-layer ($30 < y^+ < 200$), with the consideration of turbulence model using wall functions (Pope, 2000). The total grid number for the free running simulations is around 7 million and detailed grid information in each part is listed in Table 2. The motion level of the six parts of overlapping grids are also shown in Table 2.

During the simulation, the motions of propellers and rudders are treated as appendages of ship, where the grids for the propeller or rudder rotate around an axis fixed on the ship. After the grids for the appendages are transformed, the ship grids, including the propeller and rudder grids, are translated and rotated according to the 6DoF solution. Due to the hierarchical relationship, the motion level for the ship grids acts as the parent level, while the propeller and rudder grids are moved as children level to the ship grids. The background grids can move with the ship horizontally (restricted to surge, sway and yaw motions).

As for the boundary conditions of the computational domain, the inlet as shown in Fig. 1 is wave generation boundary. The conditions of velocity and volume of fraction are imposed by the specified wave theory as discussed in Section 2.3; the farfield boundaries are identical with zero velocity and zero gradient of pressure; the surfaces of the moving bodies are non-slip and the outlet is specified by the downstream boundaries.

Before starting the simulation, a simple hydrostatic computation is firstly performed to obtain the longitudinal location of the center of buoyancy, the displacement and the static wetted area of the ship in static condition. The resulting displacement of the ship model is 0.07% larger than the value used in the experiment. The small deviation is due to the spatial discretization error of the geometry. Note that artificial gaps between propellers and shafts, rudders and rudder roots are reserved to obtain enough donor cells for the overlapping grid interpolation. The positions and geometry of the rudders and propellers remain unchanged and only the shafts and rudder roots are slightly adjusted to keep the gaps. Once all the grids are generated, a preprocessing step requires setting up and running Suggar++ with appropriate boundary conditions, with the purpose of testing that valid interpolation exists.

3.3. Test conditions

The present simulations are the benchmark cases of Tokyo 2015 CFD Workshop in ship hydrodynamics. All the variables are non-dimensionalized using a reference velocity U_0 taken to be the ship service speed and the length of waterline L_{WL}. The coordinate systems for the free running model is shown in Fig. 4, where U, ψ, δ, β and χ stand for ship speed, course direction, rudder deflection angle, drift angle and incident wave angle, respectively.

According to the model tests, the fully appended ship is set to advance at model point with full 6DoF motion in both calm water and regular waves. The target ship speed is $U_0 = 1.11$ $m/s(Fr = 0.20)$ with the wave condition of $\lambda/L_{WL} = 1.0$, $H/\lambda = 0.02$, where λ is the wave length and H is the wave height. Details of test cases are shown in Table 3.

4. Free running ship models under course keeping control

The computations are carried out on a HPC cluster (IBM nx360M4) in Shanghai Jiao Tong University, which consist of 20 CPUs per node

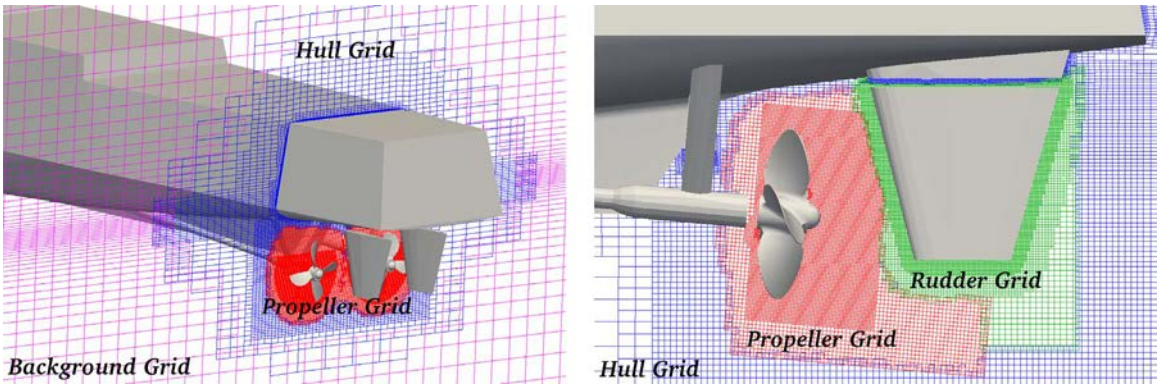

a) Transverse section b) Vertical section

Fig. 3. Overset grid distribution.

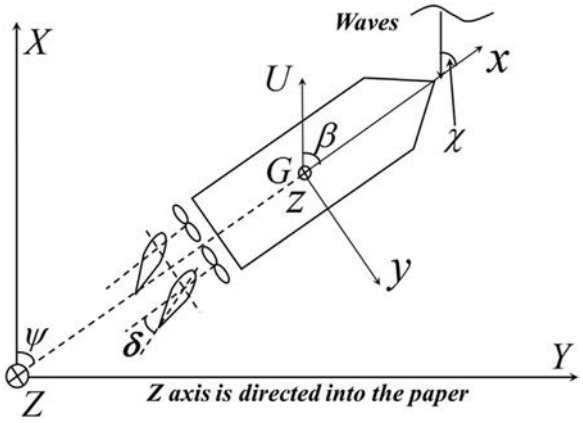

Fig. 4. Coordinate systems for free running test.

Table 3
Test conditions for course keeping simulations.

Cases		Service speed U_0 (m/s)	Wave direction χ (deg.)	Wave height H (m)	Wave length λ (m)
Calm water		1.11	NA	NA	NA
Wave	Head	1.11	0	0.06294	3.147
	Quartering	1.11	45	0.06294	3.147
	Beam	1.11	90	0.06294	3.147

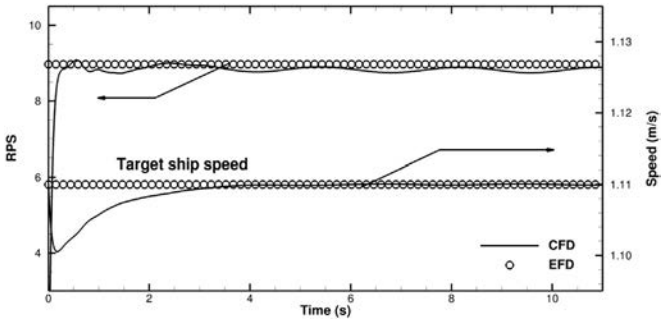

Fig. 5. Time history of ship speed and propeller rotational speed for free running in calm water.

Table 4
Comparison of model point, ship motions in calm water.

Parameters	CFD	EFD	Error
RPS (r/s)	8.819	8.97	−1.7%
Sinkage (×10² m)	0.243	0.226	6.5%
Trim (deg.)	−0.0435	−0.0386	12.7%

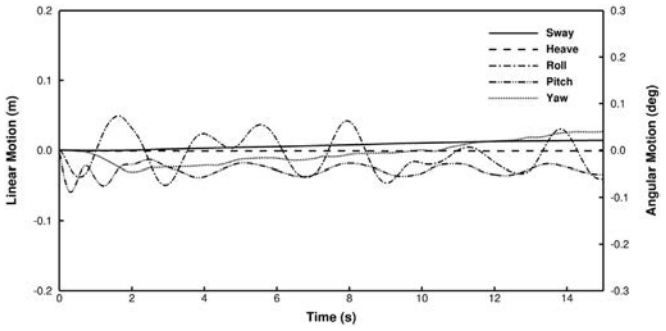

Fig. 6. Predicted ship motions for free running in calm water.

and 64 GB accessible memory (Intel Xeon E5-2680v2 @2.8 GHz). 40 processors are assigned to calculate the free running ship computation in both calm water and waves, in which 38 processors are for the flow calculation and the other 2 processors are used for DCI computation by Suggar++. The time step was set to $\Delta t = 0.0005$ s, which corresponds to approximately 1.5degs of propeller rotation per time step. Time to complete the computation was approximately 225 wall clock hours and 8979 CPU hours with about 38,000 time steps for the free running case in waves.

Due to the high computational cost and several issues with overset grid methods, a verification study has not been performed for the course keeping simulations, as has seldom been performed for the free running ship maneuvers by other researchers. The only article involved the grid studies for the free running ships is done by Carrica et al. (2016), where the grids are up to 71.3 million and the verification results show large grid uncertainties. The refining and coarsening procedure will strongly affect the overlapping grids, especially for the complex ship hull-propeller-rudder system. Despite the lack of ability in doing verification studies of free running ships, several grid uncertainty studies have been performed for simpler grid topology cases and good convergence is obtained (Shen et al., 2015; Wang et al., 2016) with the same CFD code. In the present work, extensive comparisons with experiments are performed for ship motions, trajectory, rudder angle, speeds, etc. to validate the present CFD methods.

4.1. Self-propulsion in calm water

The first simulation case is self-propulsion with full 6DoF motion under course keeping control in calm water. This case is a benchmark case in Tokyo 2015 CFD workshop in ship hydrodynamics (*Case 3.9*). First, it is used to validate the present CFD method with dynamic overset grid strategy in simulating free running ship by comparison with experimental data. Secondly, the self-propulsion computation can give the prediction of rotational speed of propeller and it is further used for the free running computations in waves.

As mentioned in Section 2.2, the rotational speed of propellers is calculated by a PI controller and the rudder is controlled by the course keeping mechanism shown in Eq. (3). The initial flow state of the self-propulsion computation is mapped from the final state of towing condition and more detailed in Wang et al. (2016). The time step was set to the same with wave cases and time to complete the computation was approximately 125 wall clock hours and 5019 CPU hours with about 24,000 time steps for the self-propulsion case in calm water.

Fig. 5 shows the time evolution of the propeller rotational speed and ship velocity. According to the result, self-propulsion in calm water at the target speed of 1.11 m/s is achieved for a propeller rotational speed of 8.819 RPS, compared to the experiment data of 8.97 RPS (shown in Table 4). The present prediction of propeller rotational speed is underestimated by 1.7%, which indicates that it is feasible to do the self-propulsion simulation using the present approach. In addition, the predicted ship speed first decreases due to less thrust provided by the rotational propellers. With the increase of RPS of propellers, the available thrust prompts the ship speed back to the target value. The accuracy of model point for free running ship model can provide a good foundation of the next free running simulations in waves.

As with the motions of other degrees of freedom (except surge motion), the amplitude is less than 0.1 m for linear motions and smaller than 0.1 degrees for angular motions as shown in Fig. 6. The predicted sinkage and trim agree well with the available experiment data (shown in Table 4).

The free surface elevation and stern view of vortical structure are presented in Fig. 7. Strong interaction between the propeller vortices and the twin rudder geometry is observed. The strong hub vortex of the propeller is rarely affected by the following rudder because the axis of the rudder is not aligned with the axis of propeller. An interesting effect occurs when the tip vortices of blades pass through the rudders, where

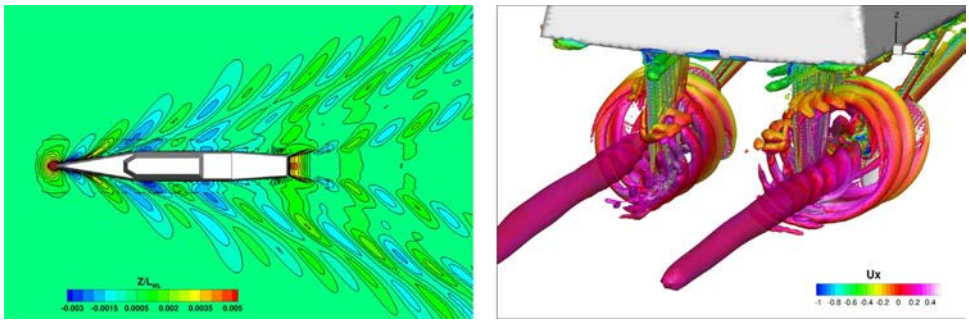

(a) Wave pattern (b) Vortical structure

Fig. 7. Flow visualizations for free running in calm water condition. (a) Wave pattern. (b) Vortical structure.

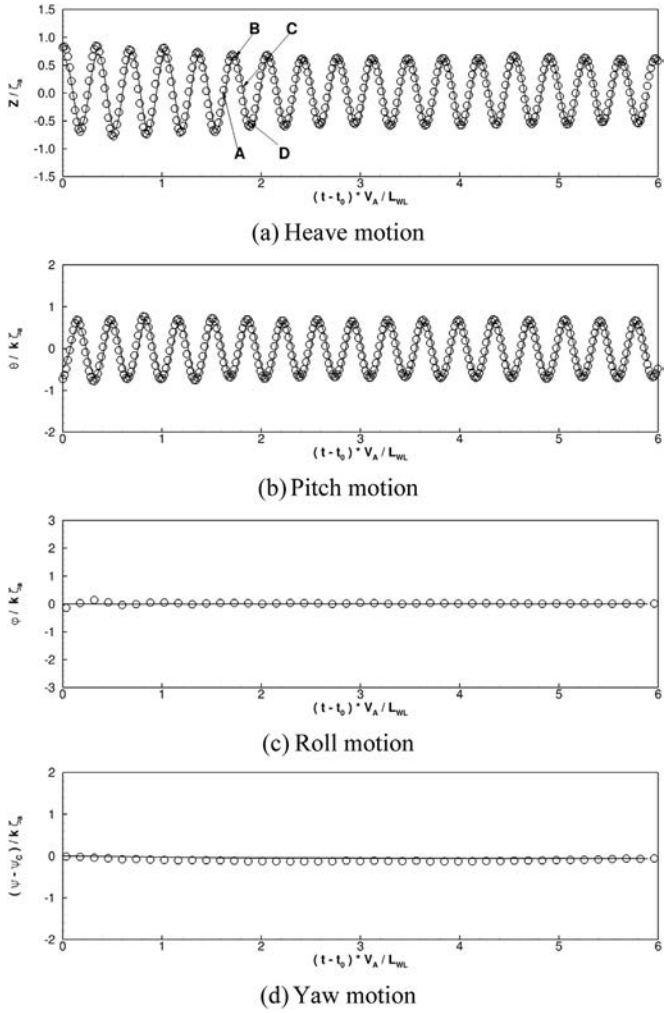

(a) Heave motion
(b) Pitch motion
(c) Roll motion
(d) Yaw motion

Fig. 8. Ship motions in head waves (A: $t = T_0$, B: $t = T_0 + 0.25T$, C: $t = T_0 + 0.5T$, D: $t = T_0 + 0.75T$).

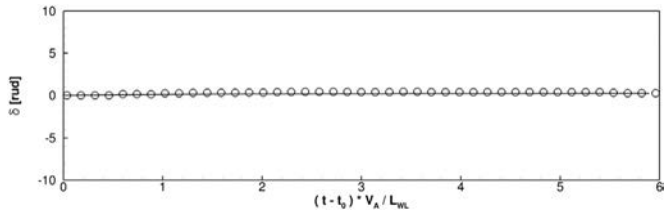

Fig. 9. Rudder deflection in head waves.

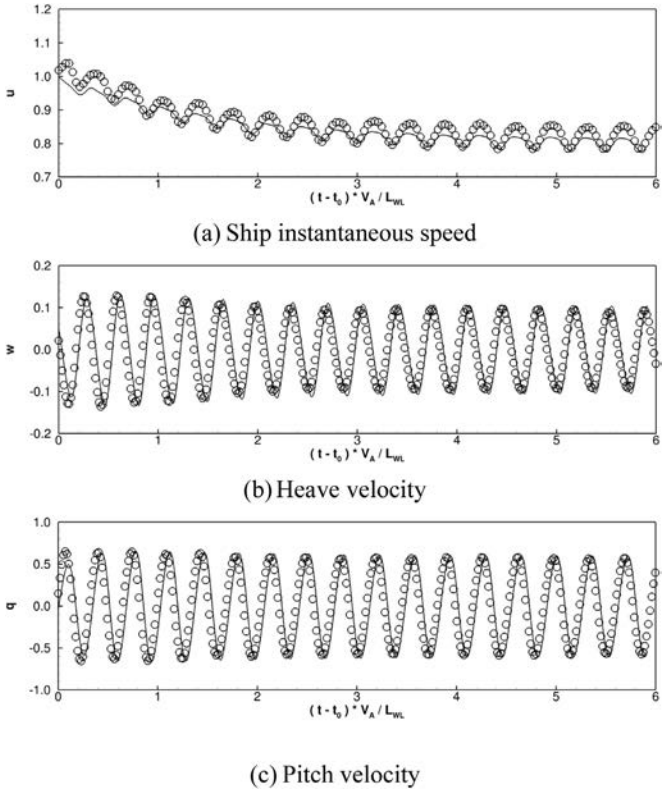

(a) Ship instantaneous speed
(b) Heave velocity
(c) Pitch velocity

Fig. 10. Time histories of ship velocities in head waves. (a) Ship instantaneous speed. (b) Heave velocity. (c) Pitch velocity.

the vortices are strongly affected by the rudder geometry both at the inward and outward side. In addition, little flow interaction is observed between the port side propeller and starboard side propeller. Strong interaction between ship hull propeller and rudder mentioned above lead to the unsteady phenomena of ship motions shown in Fig. 6.

4.2. Course keeping in waves

The free running simulation under course keeping control in waves involves three wave conditions: head wave, bow quartering wave and beam wave. This part will first present the ship motions and forces as well as the comparison with the available experiment measurements in each wave condition. Then detailed flow visualizations, e.g. wave elevation, wake profiles and vortical structures, will be discussed to further explain the hydrodynamic effects on ship performance in different incident wave conditions.

As mentioned above, free running simulation in waves adopted fixed rotational speed of propeller obtained by previous calm water CFD result. Rudders are activated under course keeping controller to

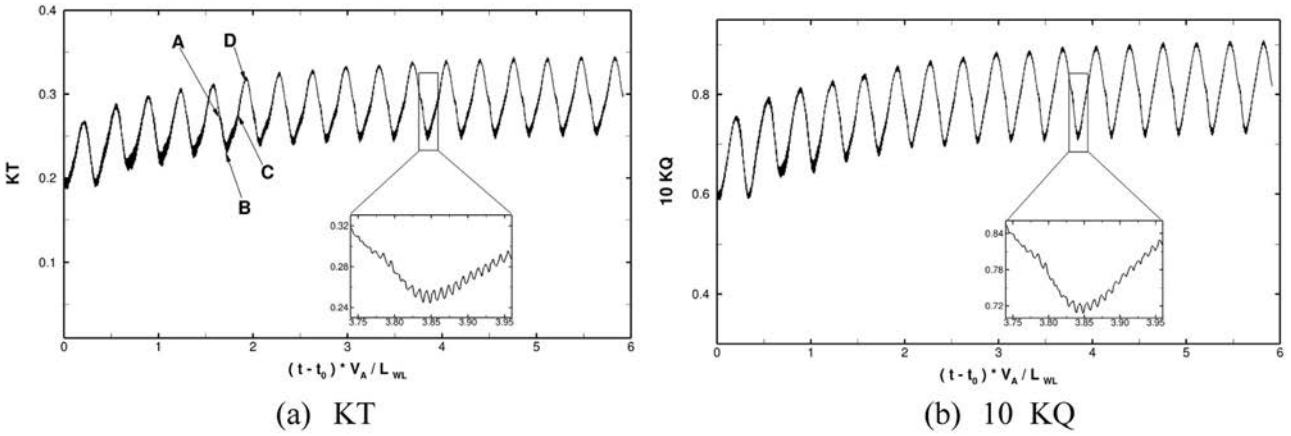

Fig. 11. Propulsion coefficients in head waves. (a) KT. (b) 10 KQ.

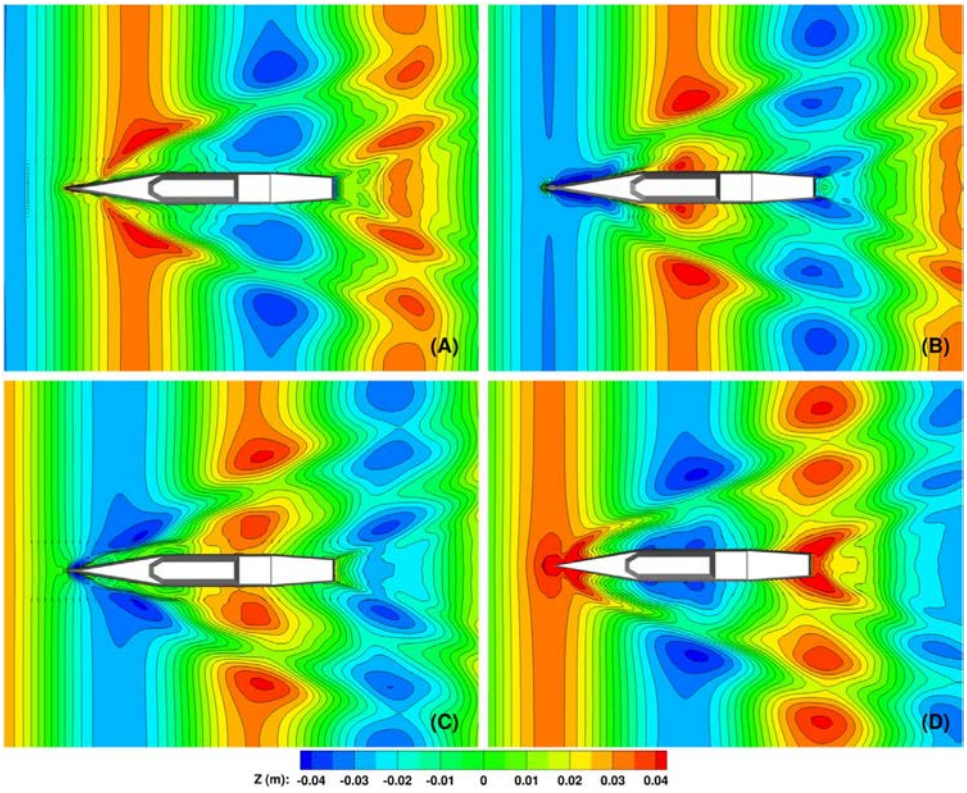

Fig. 12. Wave elevation colored with wave elevation in head waves (A: $t = T_0$, B: $t = T_0 + 0.25T$, C: $t = T_0 + 0.5T$, D: $t = T_0 + 0.75T$).

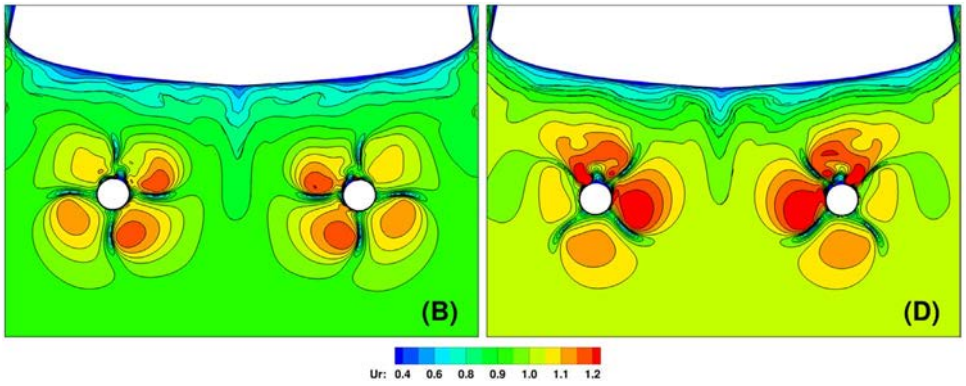

Fig. 13. Wake profiles in head waves at time instance B and D.

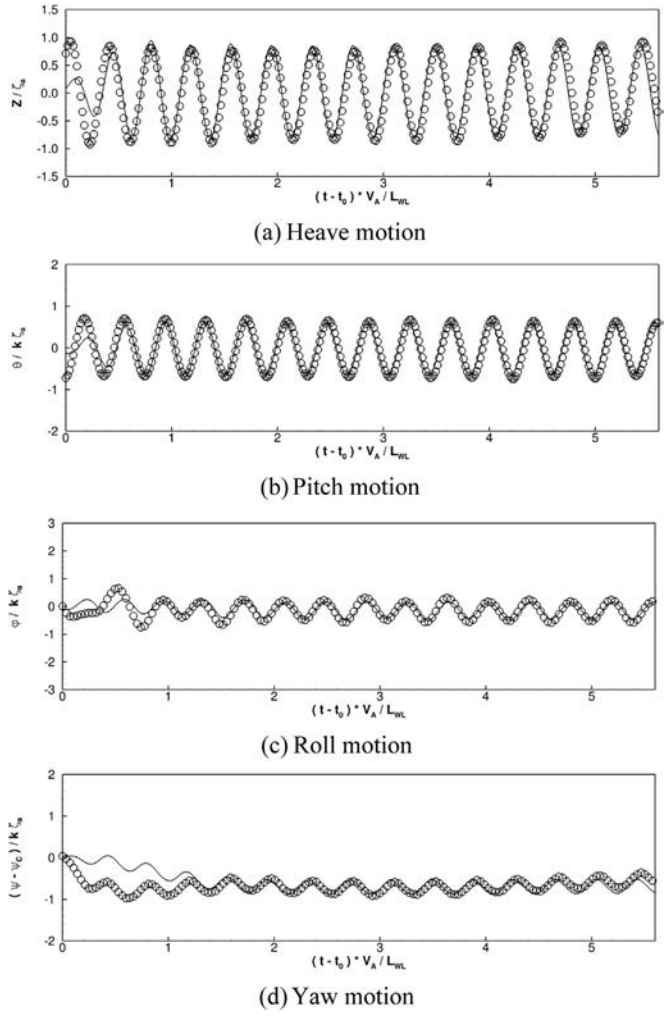

Fig. 14. Comparison of ship motions in bow quartering waves. (a) Heave motion. (b) Pitch motion. (c) Roll motion. (d) Yaw motion.

achieve the target advancing direction. Mimicking the experiment data, the simulation first started from the final state of self-propulsion in calm water and the ship is released when the wave crest is located at the bow. The general data of the CFD and EFD for ship motions and velocities are all in non-dimensional format. For the 6DOF motions $(X,\ Y,\ Z,\ \phi,\ \theta,\ \psi)$, trajectory is expressed as $(X - X_0/L_{WL},\ Y - Y_0/L_{WL})$ and time histories of heave motion is normalized by ζ_a, angular motions are presented as $(\phi/k\zeta_a,\ \theta/k\zeta_a,\ (\psi - \psi_C)/k\zeta_a)$, where k is the wave number and ζ_a is the wave amplitude. For the velocities of 6DOF motions $(u,\ v,\ w,\ p,\ q,\ r)$ are non-dimensionalized as:

$$\begin{pmatrix} u \\ v \\ w \end{pmatrix} = \frac{1}{U_0}\begin{pmatrix} \dot{x} \\ \dot{y} \\ \dot{z} \end{pmatrix} \tag{7}$$

$$\begin{pmatrix} p \\ q \\ r \end{pmatrix} = \frac{1}{\omega_e k\zeta_a}\begin{pmatrix} \dot{\phi} \\ \dot{\theta} \\ \dot{\psi} \end{pmatrix} \tag{8}$$

where ω_e is the encounter wave frequency and the unit of angular velocities $\dot{\phi}$, $\dot{\theta}$ and $\dot{\psi}$ is rad/s. Rudder angle δ is in degrees and propulsion coefficients are expressed as:

$$KT = \frac{T}{\rho n^2 D_P^4} \tag{9}$$

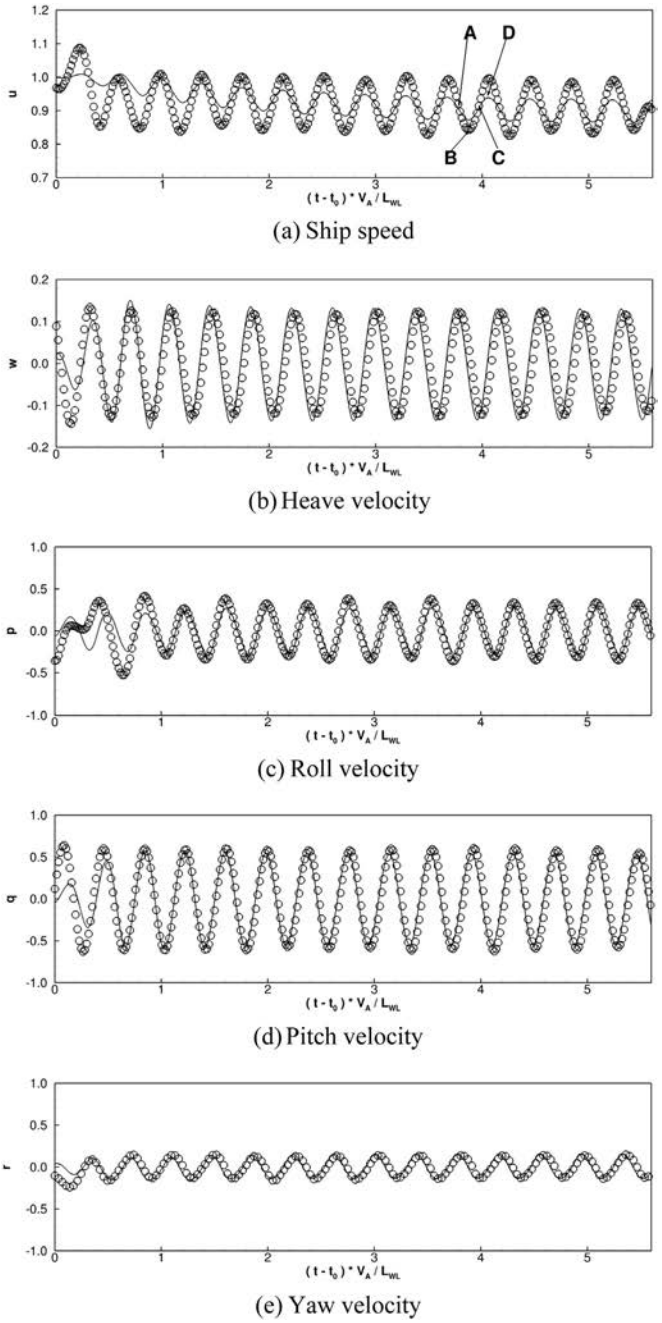

Fig. 15. Comparison of ship velocities in bow quartering waves. (a) Ship speed. (b) Heave velocity. (c) Roll velocity. (d). Pitch velocity. (e) Yaw velocity.

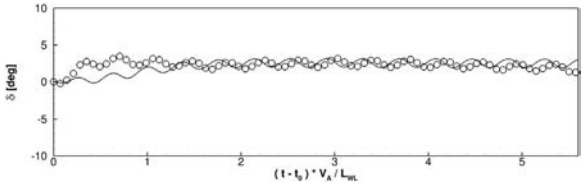

Fig. 16. Rudder deflection.

$$KQ = \frac{Q}{\rho n^2 D_P^5} \tag{10}$$

where T and Q are the thrust and torque of rotating propellers; n is the rotational speed of propeller; D_P is the diameter of propeller. In all figures of the comparison with the experiments shown afterwards, solid lines represent the present CFD results and circles stand for the

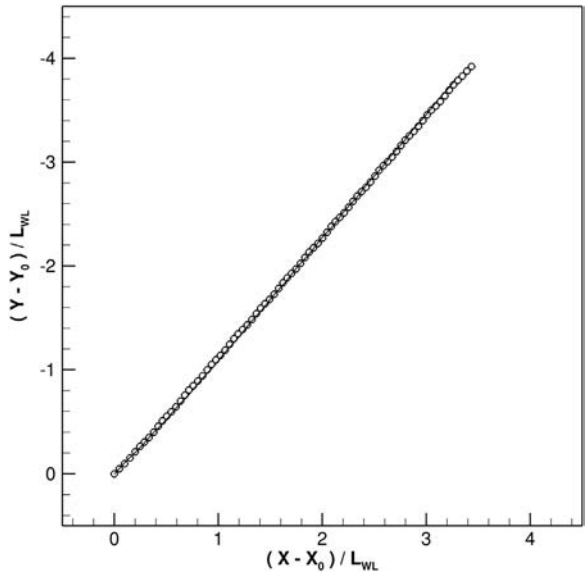

Fig. 17. Trajectory comparison in bow quartering waves.

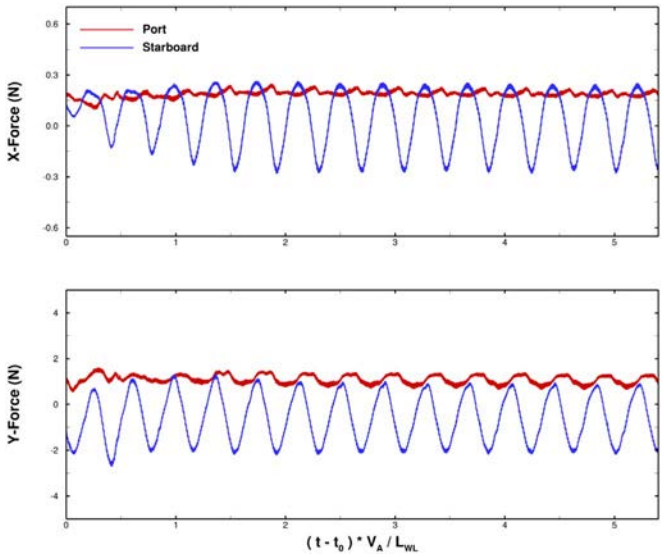

Fig. 19. Comparison of port side and starboard rudder forces.

experimental data unless otherwise stated. In addition, Fourier Series (*FS*) (Shen and Wan, 2013; Tezdogan et al., 2015) are used to quantitative analyze the unsteady time histories of the ship motions and velocities due to waves.

4.2.1. Head waves

Fig. 8 shows the simulation results of the time evolution of ship motions in head waves. The predicted heave and pitch motions show overall agreement with the experimental results, with the 1st harmonic *FS* term of heave and pitch motions underestimated by 3.7% and 2.8% respectively. As for the roll motion and yaw motion, both predicted and measured data show approximate no fluctuation due to the head wave condition. In addition, the rudder deflection (Fig. 9) shows that it is not a major concern to keep the ship advancing straight forward in head waves.

Fig. 10 illustrates the considerable ship velocities, i.e. advancing speed, heave velocity and angular velocity of pitch motion, during the simulation time. For the ship speed u, the curves show evident speed loss mainly affected by the added resistance induced by the incident waves both in numerical and experimental result. And the speed loss, which can be measured by 0th harmonic *FS* term of u, is about 17%. The present result matches well with the overall trend of the measurement, while the mean fluctuation amplitude (1st harmonic *FS* term) is underestimated by 46%. As opposed to the CFD simulations that were performed at constant propeller rotational speed, the propellers in the experiments were subject to the changing hydrodynamic load, and exhibit a change of propeller rotational speed (Mofidi et al., 2016). This can be one of the reasons to explain the discrepancy. Besides, the ship speed is mainly determined by the ship resistance and propeller thrust. However, the lack of experiment data for forces and moments of ship hull, propellers and rudders prevent the comparison and this phenomenon needs further investigation. Heave and pitch velocities show the same trend with the corresponding motions and the comparison also matches well with the experiment data. The overall agreement shows that the present approach can predict the motion response with high accuracy.

To further analyze the propulsive performance, the predicted propulsion coefficients, i.e. KT and $10KQ$, are presented in Fig. 11. Both thrust and torque coefficients are evidently related to the time evolution of ship motions. The thrust coefficient achieves maximum when the ship bow goes up and reaches minimum with the bow goes down. The same trend occurs with the torque coefficients. The variation of propulsion coefficients shows consistency with the speed loss presented in Fig. 10a. For instance, at time B, the actual ship speed is larger and result in larger inflow of the propeller, which further leads to the decrease of thrust. Better understanding of this phenomenon will be shown in the following flow visualizations. Besides, high frequency fluctuations in thrust and torque coefficients that correlate to the blade passage frequency are observed in the predicted results, which can be clearly seen in the partial enlarged view.

Though experiments are still playing an important role on the free running tests, CFD is becoming undeniably attractive for the numerical analysis and visualizations of the flow field. Four typical time instances in one wave period, where A, B, C, and D corresponding to the time

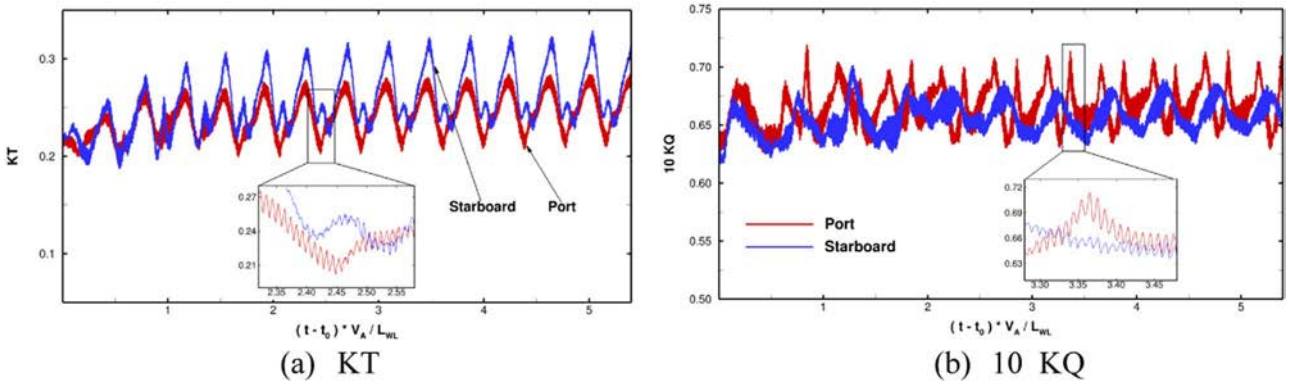

Fig. 18. Propulsion coefficients in bow quartering waves (10 KQ value in starboard side is mirrored for better comparison with port side). (a) KT. (b) 10 KQ.

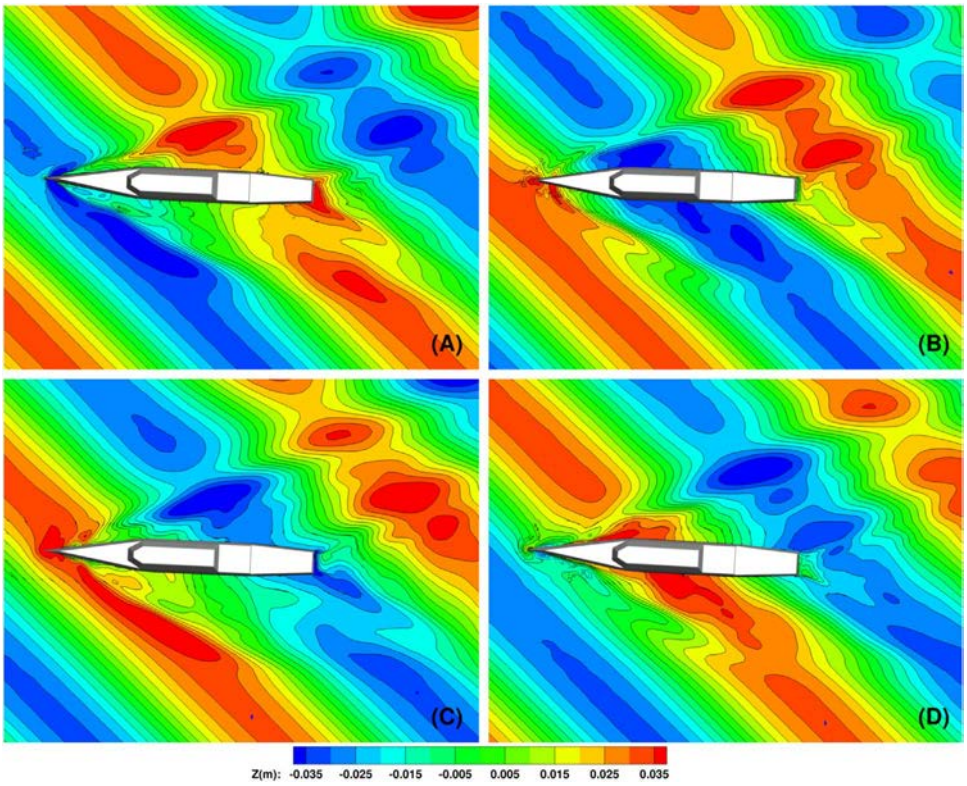

Fig. 20. Wave elevation in one wave period for bow quartering waves.

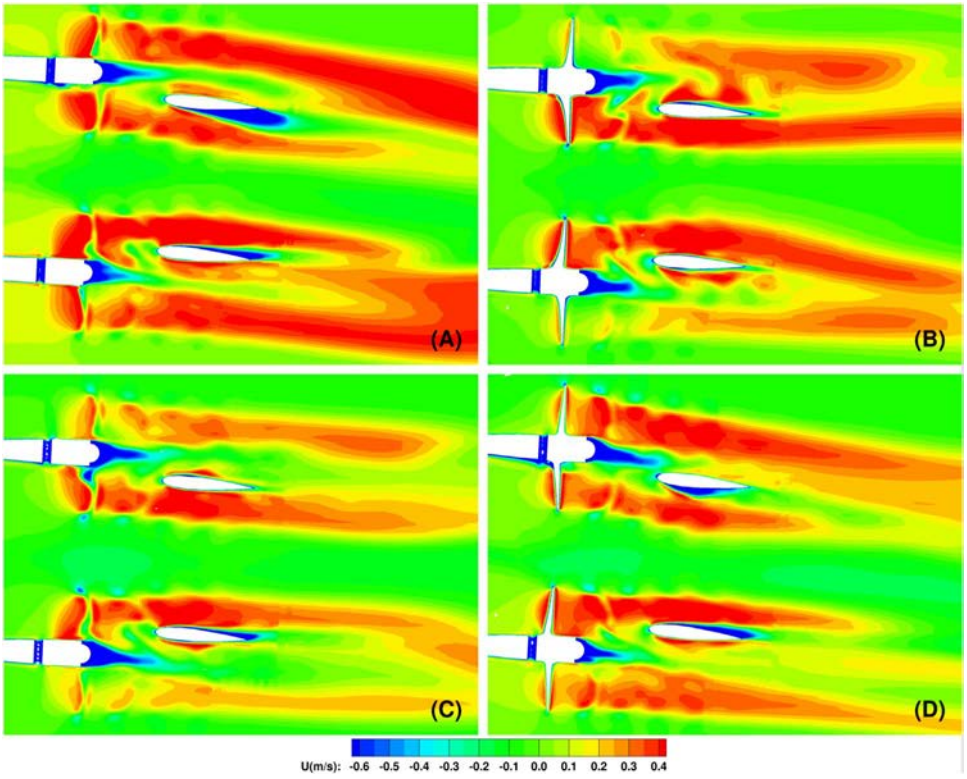

Fig. 21. Wake regions around twin propellers and twin rudders in one wave period.

shown in Fig. 8a, are chosen to further analyze the hydrodynamic performance of the free running ship in head waves.

Fig. 12 shows four instantaneous snapshots of free surface in one wave period. An interesting phenomenon was observed that when the forehead of ship bows down (time D), a new wave crest occurs after the incident wave crest. To further explain the propulsion performance of thrust and torque, a wake profile ahead of twin propellers is presented in Fig. 13. Two snapshot corresponding to time instance B and D are shown. The flow field is colored by the relative axial velocity $U_r = U_0 - U_x$ for better visualization. The relative inflow at time B is

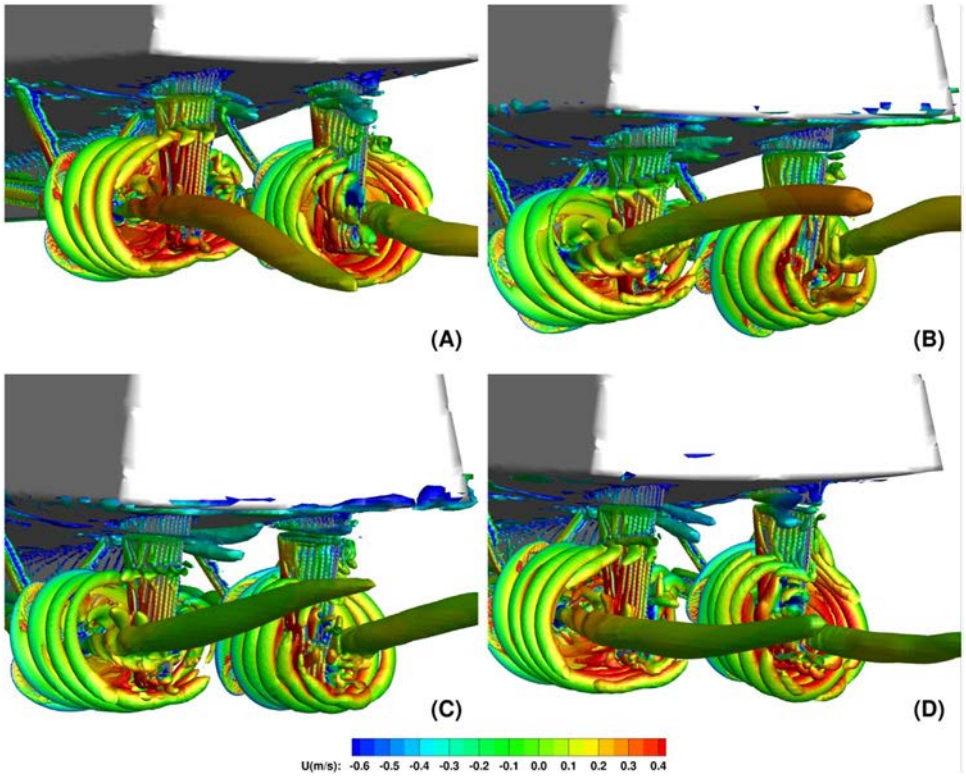

Fig. 22. Vortical structures around twin propellers and rudders depicts as Q=200 colored by axial velocity in one wave period.

obviously smaller than that of time D, which means that the actual inflow is in the opposite way. This gives a better understanding of the variation of propulsive coefficients explained in the previous part.

4.2.2. Bow quartering waves

The predicted ship motions in bow quartering waves and the comparison with experiment are shown in Fig. 14. Heave and pitch motions experience the same trend as in the head wave conditions and match well with the experimental measurement, while the roll and yaw motions show larger fluctuations. The non-dimensional roll motion can be up to 0.6 with the roll angle of 20.2°. The yaw motion is even larger than roll motion, where the non-dimensional yaw motion is 0.89 with the yaw angle of 30.2°. This is mainly because that large lateral force and yaw moment can be induced by the incident quartering waves. The present CFD approach is able to well predict these phenomena and shows good correlation with the experiment.

Fig. 15 illustrates the ship speeds in quartering waves. The speed loss is 9%, smaller than that of 17% in head waves (shown in Fig. 10a). This is because the oblique wave causes force redistribution around ship hull and less added resistance in sailing direction. CFD results show smaller fluctuation than experimental measurement with the 1st harmonic *FS* term of u under predicted by 58%. As for the linear velocity of heave motion and angular velocity of pitch, roll and yaw motion, the predicted results matches well with the experiment, though little discrepancy can be observed at the beginning of the simulation. Good agreement of predicted ship motions can also be explained by the present satisfactory result of velocities.

The rudder deflection as shown in Fig. 16 becomes a significant process to keep the ship advancing straight forward in bow quartering waves. The maximum execution angle of the rudders is about 3.2 degrees. Since the course keeping controller is directly dependent on the yaw deviation angle, the rudder angle show an exact same trend as the yaw motion presented in Fig. 14d. In addition, the predicted rudder angle matches well with the experimental measurement except for the rudder deflection at first several periods.

Fig. 17 shows the trajectory comparison between present CFD results and experimental data. Complex as the problem may appear, the predicted trajectory shows remarkable good agreement with the free running tests. It further indicates that CFD approach to simulate the free running ship model under course keeping control is feasible and the implementation of the developed course keeping module is reliable.

The predicted propulsion coefficients, i.e. KT and $10KQ$, are presented in Fig. 18. Different from the head wave conditions, both port and starboard thrust and torque coefficients are presented with the consideration of the strong asymmetry of the inflow velocity. The thrust coefficient of the starboard propeller is larger than that of the port side propeller for almost all the time. This can be explained by the different inflow for twin propellers in bow quartering waves and this can be better understood from the flow visualizations shown later. The torque coefficients also show difference for both side propellers. Similarly, the variation of propulsion coefficients are strong related to the advancing ship speed presented in Fig. 15a. For instance, at time instant B, the actual ship speed is smaller and result in smaller inflow of the propeller, which will further lead to the increase of thrust. Furthermore, high frequency fluctuations in thrust and torque coefficients that correlate to the blade passage frequency are observed in the predicted results, which can be obviously seen in the partial enlarged view.

Fig. 19 illustrates the rudder forces for port and starboard side in both X and Y directions. It can be clearly seen that the starboard side rudder has larger amplitude of oscillations during the simulation in bow quartering waves. This phenomenon shows correspondence to the propulsion coefficient KT in Fig. 18a. The rudder execution due to the course keeping control can also result in the large discrepancy of the flow field around twin rudders and further affect the propulsion coefficients shown in Fig. 18. In order to explain the highly different performance for twin propellers and rudders, four typical time instances have been chosen in one wave period, i.e. A, B, C, and D shown in Fig. 15a to analyze the flow characters.

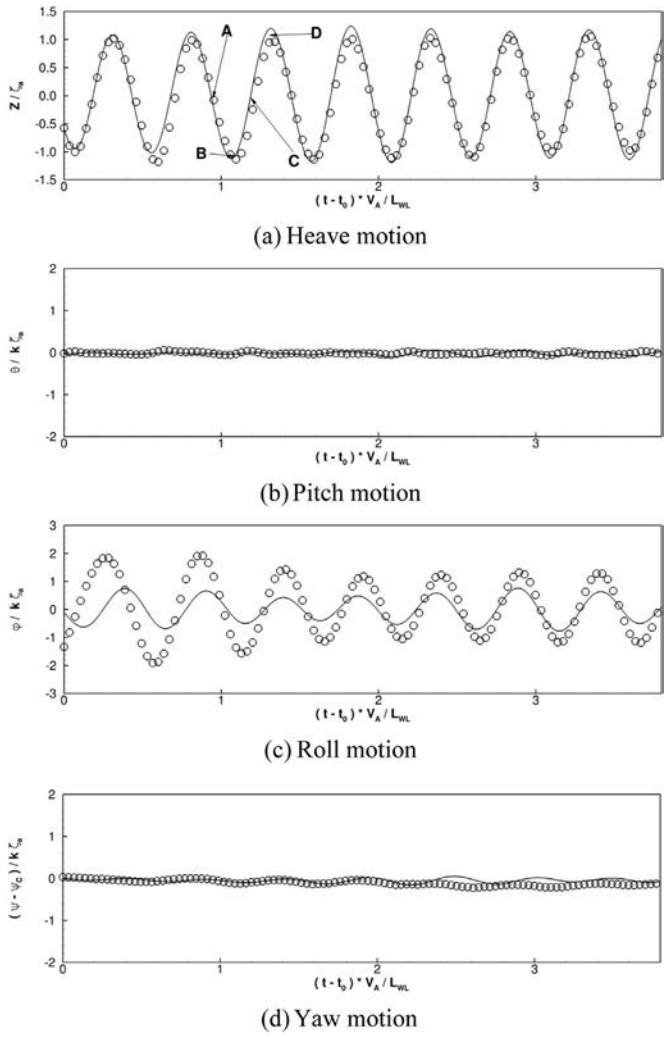

Fig. 23. Comparison of ship motions in beam waves. (a) Heave motion. (b) Pitch motion. (c) Roll motion. (d) Yaw motion.

Fig. 20 shows four snapshots of wave elevation in one wave period. The wave profiles around ship hull show asymmetry, which induces significant lateral force and yaw moment. In addition, the ship wave making is considerable in the present ship speed with incident waves. Moreover, the wave profiles in windward side and leeward side are highly different due to the interaction between incident waves and the ship waves. The direction of propagation of windward side ship wave is opposite to incident wave, while the leeward side wave propagates along with the incident wave.

Fig. 21 shows the wake region around twin propellers and rudders in a horizontal section across the propeller center. The flow field around starboard side propeller and rudder is more complex than that of the port side. This can give a better explanation for the discrepancy of hydrodynamic forces acted on the propellers and the rudders shown in Figs. 18 and 19.

Fig. 22 illustrates four snapshots of vortical structures around twin propellers and rudders colored by axial velocity in one wave period. Vortices are represented as iso-surfaces of Q=200. Strong tip and hub vortex can be observed for the twin rotating propellers. The interaction of the propeller tip and hub vortices with aligned rudder are evident in the views shown in Fig. 22, where at time instance B and C, the hub vortices of the port side propeller are strongly affected by following rudder, while the phenomenon shows the opposite way at time instances A and D. Furthermore, the shapes of hub vortices show close relations with the corresponding ship motions in waves. An interesting

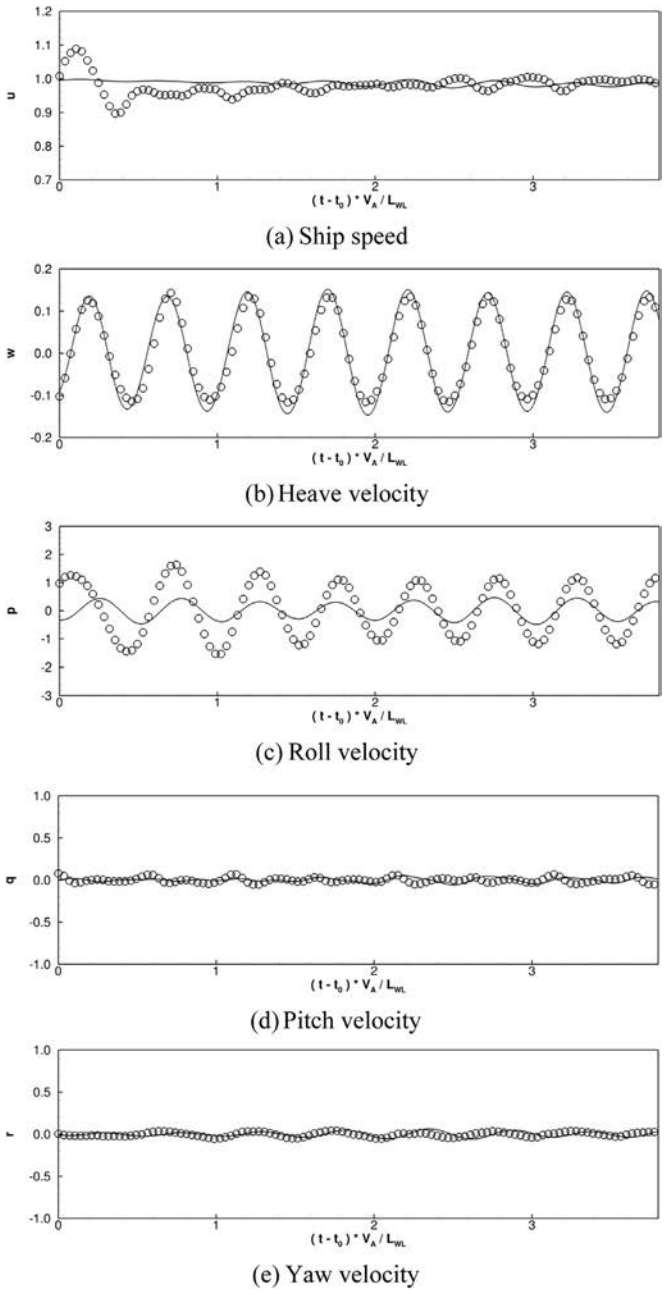

Fig. 24. Ship velocities in beam waves. (a) Ship speed. (b) Heave velocity. (c) Roll velocity. (d) Pitch velocity. (e) Yaw velocity.

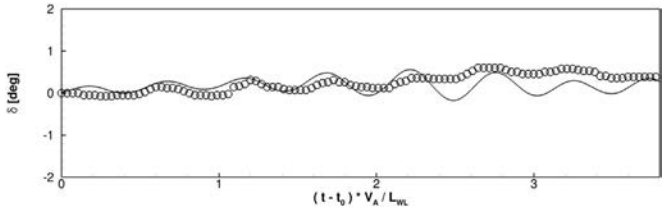

Fig. 25. Rudder deflection in beam waves.

phenomenon is that the rudder root vortices are also evident due to the artificial gap between rudders and ship hull in overset grid methodology.

4.2.3. Beam waves

The comparison of predicted ship motions with experiment in beam

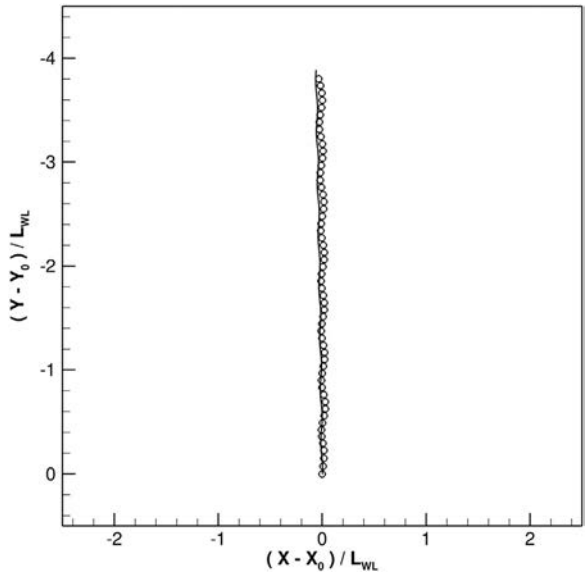

Fig. 26. Trajectory comparison in beam waves.

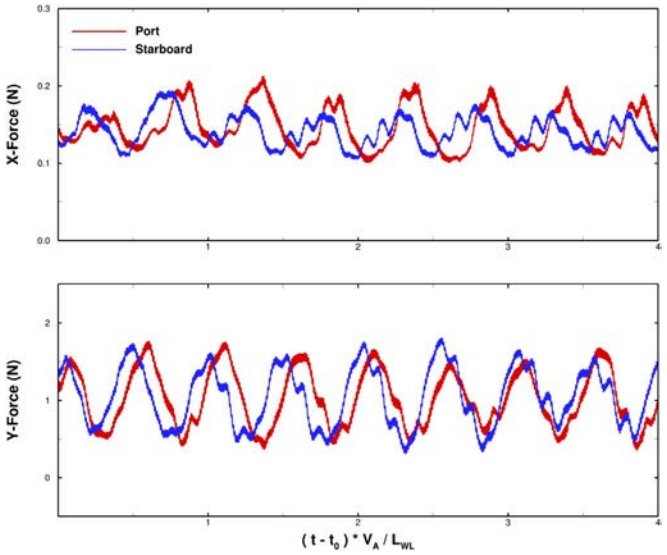

Fig. 28. Comparison of port and starboard rudder forces in beam waves (Starboard Y-Force is mirrored for better comparison with port side force).

waves are shown in Fig. 23. Heave motion agrees well with the experiment with 1st harmonic *FS* term of heave motion in beam waves is overestimated by 8.9%. Although the pitch motion in beam waves is very small compared with the head wave and quartering wave conditions, this phenomenon can be captured by both CFD and experimental measurement. The roll motion in beam waves shows the largest fluctuations among all the wave conditions with the non-dimensional roll motion up to 1.9 and roll angle up to 60.8°. Incident beam waves cause the significant difference of pressure distribution around the windward and leeward side, which further leads to the large roll motion. The difference with the initial state of the roll motion and the inaccurate rotational center can explain the large discrepancy with the experiment. The present simulation adopt the rotational center just as the same with vertical center of gravity (shown in Table 1), since no experimental data for the rotational center is available. As for the yaw motion, smaller fluctuations are observed compared with the bow quartering wave conditions, where the maximum non-dimensional yaw motion is 0.19 compared with 0.89 in bow quartering waves. This indicates that the beam wave can hardly affect the head angle of a free running ship. Though little discrepancy exists, the present CFD results can generally describe the motion response in beam wave conditions.

Fig. 24 illustrates the ship velocities during beam waves. Compared with the former wave conditions, the speed loss is only 2% with the fact that the beam wave can hardly affect the force distribution in advancing direction. CFD results for the heave velocity, pitch velocity and yaw velocity experience the same trend with the corresponding motions and matches well with the measurement. However, the roll velocity has large discrepancy with the beginning value and amplitude, which further results in the difference of the roll motion.

The rudder deflection (shown in Fig. 25) in beam waves shows that it is not a significant process to keep the ship advancing straight forward. The maximum execution angle of the rudders is less than 0.5 degrees. Since the course keeping controller is strongly dependent on the yaw deviation angle, the rudder angle shows a similar trend of the yaw motion presented in Fig. 23d. In addition, the predicted rudder angle shows an overall agreement with the experimental measurement except for the larger amplitude fluctuations.

Fig. 26 shows the comparison of trajectory between present CFD result and experimental data in beam wave conditions. Similarly, the predicted trajectory shows remarkable good agreement with the free running tests. Trajectory in experiment deviate from the original path a little more than that of the present CFD result. This can be explained as follows, the yaw motion of the experiment measurement shown in Fig. 23d keeps negative value while the CFD result oscillates around zero, which will further lead to the deviation in the trajectory.

The predicted propulsion coefficients are shown in Fig. 27. Unlike the head wave and bow quartering wave conditions, thrust coefficient shows smaller fluctuations on both port side and starboard side propeller. The range of the thrust coefficient in beam wave is from 0.2 to 0.25, much smaller than the variation of 0.19–0.35 in head wave and 0.19–0.32 in bow quartering wave. This can be explained by the instantaneous ship speed (actual inflow) shown in Fig. 24a, where the ship speed in beam waves is larger than that of the head wave and quartering wave conditions. Larger advancing speed result in the larger

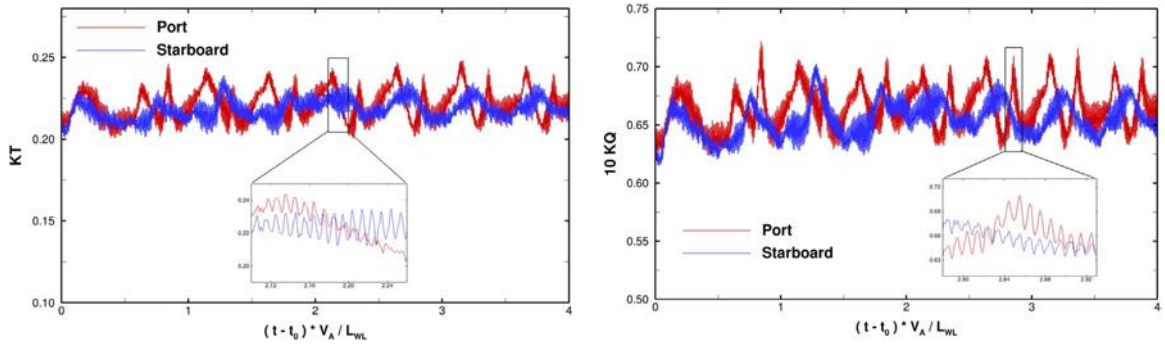

(a) KT (b) 10 KQ

Fig. 27. Propulsion coefficients in beam waves (10 KQ value in starboard side is mirrored for better comparison with port side value). (a) KT. (b) 10 KQ.

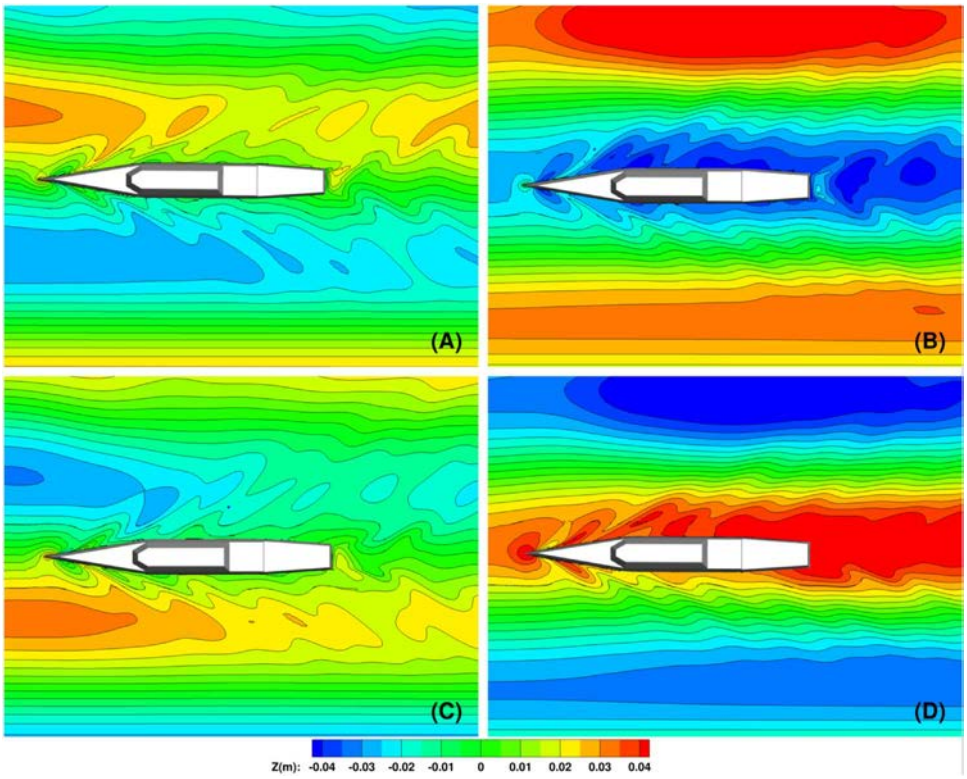

Fig. 29. Wave elevation in one wave period.

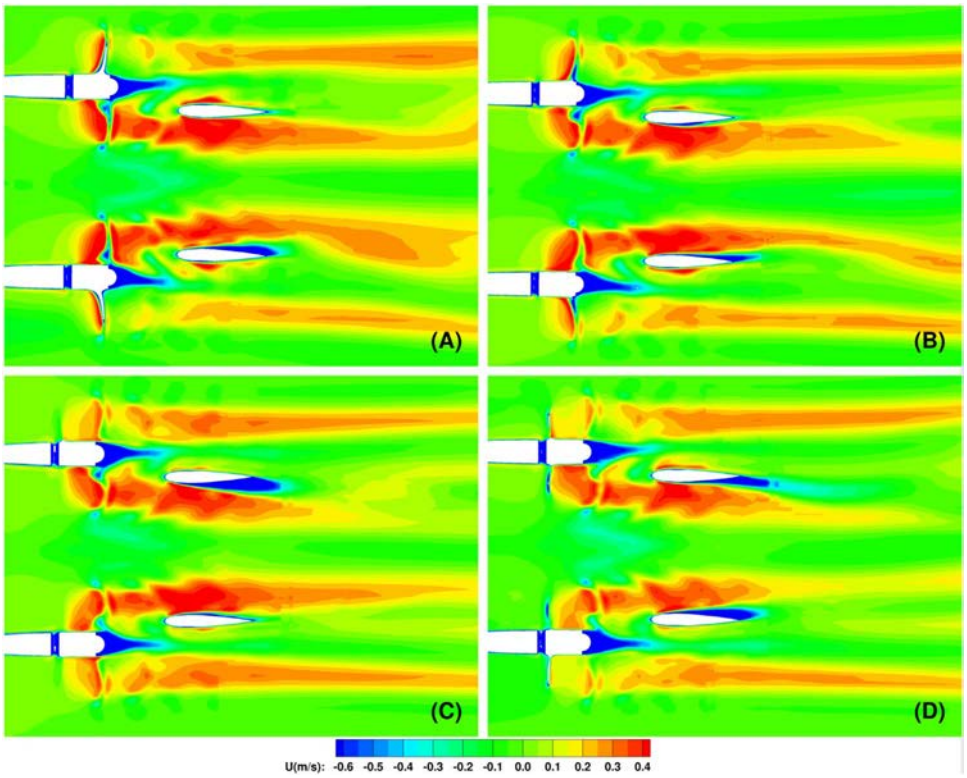

Fig. 30. Wake region around twin propellers and rudders.

advance coefficient J, which further reduce the thrust. The thrust and torque coefficients of port side propeller show larger fluctuations than the starboard side due to the complex inflow of the windward propeller. Furthermore, high frequency fluctuations in thrust and torque coefficients that correlate to the blade passage frequency are also observed in the predicted results, which can be obviously seen in the partial enlarged view.

Fig. 28 illustrates the forces of the twin rudders in X and Y directions. Similarly, the X-force of the windward side rudder experiences larger variations in beam waves, while the amplitude of rudder

force in Y direction is almost the same.

In order to explain the highly different performance for twin propellers and rudders, four typical time instances in one wave period, i.e. A, B, C, and D shown in Fig. 24a are chosen to analyze the flow characters. Fig. 29 depicts the wave elevation colored by wave height in one beam wave period. Different from the head wave and bow quartering wave conditions, the wave elevation show significant difference within one period, where the wave height at time instances B and D are bigger than that of time instances A and C. In other words, the wave height are bigger when the ship experiences the wave crest or trough. This is mainly due to the stack effect of ship wave making and the incident beam wave. In addition, the ship wave making in windward side is disturbed by the incident wave while the leeward side wave propagates along with the beam wave to a larger range.

Fig. 30 illustrates the horizontal section of wake region around twin propellers and rudders colored by axial velocity. The inflow of the twin propellers at the four typical time instants show less discrepancy and can explain the thrust performance shown in Fig. 27. Furthermore, the windward propeller wake region is strongly affected by the incident beam wave, where the trajectory of the tip vortices moves to the leeward side. Asymmetric flow around the twin rudders can also explain the difference of hydrodynamic performance between port and starboard sides in beam waves as shown in Fig. 28.

5. Conclusions and future work

This paper discusses the direct simulations of free running ship model under course keeping control in both calm water and regular waves using the CFD solver naoe-FOAM-SJTU. Fully appended ONR Tumblehome ship model is employed for the validation studies. With the capability of dynamic overset grids, the full 6DoF motion solver with a hierarchy of bodies are applied to calculate the complex ship motions with actual rotating propellers and moving rudders in a rough free surface environment. A feedback course keeping control module is developed to simulate free running ship under course keeping control and self-developed 3D wave generate module is applied to generate desired wave conditions.

Self-propulsion calculations are performed firstly as needed to obtain the model point for CFD simulations, where the predicted rotational speed of propellers is underestimated only by 1.7%. Free running ship in three incident waves, i.e. head waves, bow quartering waves and beam waves, are simulated and extensive comparisons with experiments are performed for ship motions, trajectory, speeds, etc. to validate the present CFD results. The predicted trajectory for all the cases show remarkable good agreement with the free running tests, which further indicates that the implementation of course keeping controller is applicable. The speed loss is about 17% in head waves, while for bow quartering waves and beam waves, the speed loss drops to 9% and 2% respectively. Bow quartering waves experience the largest yaw deviation and maximum rudder execution is 3.2 degrees. Thus, course keeping can be a main factor when a ship is sailing in oblique waves. Propulsion coefficients, i.e. KT and 10 KQ, as well as the rudder forces are presented to illustrate the hydrodynamic performance during free running ship in waves. Flow visualizations, such as wave elevations, wake region around twin propellers and rudders, vortical structures, are presented to give better description of the flow characters during the free running ship in waves.

The main conclusion of the work presented in this paper is that the present CFD solver naoe-FOAM-SJTU coupled with the newly developed course keeping module can be effectively used to handle problems with free running ship under course keeping control. Moreover, the CFD simulations of free running ships have been extended from calm water to various heading waves. Though CFD is undeniable attractive to perform free running ship simulations, the computational cost is still very high (about two weeks to complete one simulation case).

Future work includes simulations of standard ship maneuvers, such as turning circle maneuver and zigzag maneuver, in different heading waves.

Acknowledgments

This work is supported by the National Natural Science Foundation of China (51490675, 51379125, 11432009, 51579145), Chang Jiang Scholars Program (T2014099), Shanghai Excellent Academic Leaders Program (17XD1402300), Shanghai Key Laboratory of Marine Engineering (K2015-11), Program for Professor of Special Appointment (Eastern Scholar) at Shanghai Institutions of Higher Learning (2013022), and Innovative Special Project of Numerical Tank of Ministry of Industry and Information Technology of China (2016-23/09), to which the authors are most grateful.

References

Araki, M., Sadat-Hosseini, H., Sanada, Y., Tanimoto, K., Umeda, N., Stern, F., 2012. Estimating maneuvering coefficients using system identification methods with experimental, system-based, and CFD free running trial data. Ocean Eng. 51, 63–84.

Broglia, R., Dubbioso, G., Durante, D., Di Mascio, A., 2015. Turning ability analysis of a fully appended twin screw vessel by CFD. Part I: single rudder configuration. Ocean Eng. 105, 275–286.

Cao, H., Wan, D.C., 2015. RANS-VOF solver for solitary wave run-up on a circular cylinder. China Ocean Eng. 29 (2), 183–196.

Cao, H., Wan, D.C., 2014. Development of Multidirectional nonlinear Numerical wave tank by naoe-foam-SJTU solver. Int. J. Ocean Syst. Eng. 4, 52–59.

Carrica, P.M., Castro, A.M., Stern, F., 2010. Self-propulsion computations using a speed controller and a discretized propeller with dynamic overset grids. J. Mar. Sci. Technol. 15, 316–330.

Carrica, P.M., Mofidi, A., Eloot, K., Delefortrie, G., 2016. Direct simulation and experimental study of zigzag maneuver of KCS in shallow water. Ocean Eng. 112, 117–133.

Castro, A.M., Carrica, P.M., Stern, F., 2011. Full scale self-propulsion computations using discretized propeller for the KRISO container ship KCS. Comput. Fluids 51, 35–47.

Dubbioso, G., Durante, D., Di Mascio, A., Broglia, R., 2016. Turning ability analysis of a fully appended twin screw vessel by CFD. Part II: single vs. twin rudder configuration. Ocean Eng. 117, 259–271.

International Maritime Organization, 2002. Standards for Ship Maneuverability. MSC 137, 76.

Issa, R.I., 1986. Solution of the implicitly discretised fluid flow equations by operator-splitting. J. Comput. Phys. 62, 40–65.

Menter, F.R., Kuntz, M., Langtry, R., 2003. Ten years of industrial experience with the SST turbulence model. Turbul. Heat. Mass Transf. 4, 625–632.

Mofidi, A., Carrica, P.M., 2014. Simulations of zigzag maneuvers for a container ship with direct moving rudder and propeller. Comput. Fluids 96, 191–203.

Mofidi A., Castro A., Carrica P.M., 2016. Self-propulsion and course keeping of ONR Tumblehome in calm water and waves. In: Proceedings of Tokyo 2015 CFD Workshop in ship hydrodynamics, vol III, pp 303–308.

Noack, R.W., Boger, D.A., Kunz, R.F., Carrica, P.M., 2009. Suggar++: An improved general overset grid assembly capability, In: Proceedings of the 19th AIAA Computational Fluid Dynamics Conference, San Antonio TX, pp. 22–25.

OpenFOAM , 2016. The OpenFOAM Foundation. URL ⟨http://openfoam.org/⟩ (accessed 4 November 2016).

Pope, S.B., 2000. Turbulent Flows. Cambridge University Press, 273–274.

Sakamoto, N., Carrica, P.M., Stern, F., 2012. URANS simulations of static and dynamic maneuvering for surface combatant: part 2. analysis and validation for local flow characteristics. J. Mar. Sci. Technol. 17, 446–468.

Sanada, Y., Tanimoto, K., Takagi, K., Gui, L., Toda, Y., Stern, F., 2013. Trajectories for ONR Tumblehome maneuvering in calm water and waves. Ocean Eng. 72, 45–65.

Shen, Z., Cao, H., Ye, H., Wan, D.C., 2012. The manual of CFD solver for ship and ocean engineering flows: naoe-FOAM-SJTU. No. 2012SR118110. Shanghai Jiao Tong University.

Shen, Z., Wan, D.C., 2016. An irregular wave generating approach based on naoe-FOAM-SJTU solver. China Ocean Eng. 30 (2), 177–192.

Shen, Z., Wan, D.C., 2013. RANS computations of added resistance and motions of a ship in head waves. Int. J. Offshore Polar Eng. 23 (4), 264–271.

Shen, Z., Wan, D.C., Carrica, P.M., 2015. Dynamic overset grids in OpenFOAM with application to KCS self-propulsion and maneuvering. Ocean Eng. 108, 287–306.

Shen, Z., Ye, H., Wan, D.C., 2014. URANS simulations of ship motion responses in long-crest irregular waves. J. Hydrodyn. 26 (3), 436–446.

Simonsen, C.D., Otzen, J.F., Klimt, C., Larsen, N.L., Stern, F., 2012. Maneuvering predictions in the early design phase using CFD generated PMM data, In: Proceedings of the 29th Symposium on Naval Hydrodynamics, Gothenburg, Sweden, pp. 26–31.

Tezdogan, T., Demirel, Y.K., Kellett, P., Khorasanchi, M., Incecik, A., Turan, O., 2015. Full-scale unsteady RANS CFD simulations of ship behaviour and performance in head seas due to slow steaming. Ocean Eng. 97, 186–206.

Wang, J., Zhao, W., Wan, D.C., 2016. Free Maneuvering Simulation of ONR Tumblehome Using Overset Grid Method in naoe-FOAM-SJTU Solver, In: Proceedings of 31th Symposium on Naval Hydrodynamics, Monterery, USA.

Weller, H.G., 2008. A new approach to VOF-based interface capturing methods for incompressible and compressible flow. Open. Ltd Rep., (TRHGW04).

Zha, R., YE, H., SHEN, Z., WAN, D.C., 2015. Numerical computations of resistance of high speed catamaran in calm water. J. Hydrodyn. 26 (6), 930–938.